



Article

Characteristics of Raindrop Size Distributions in the Southwest Mountain Areas of China According to Seasonal Variation and Rain Types

Haopeng Wu ¹, Shengjie Niu ^{1,2,*}, Yue Zhou ³, Jing Sun ³, Jingjing Lv ¹ and Yixiao He ⁴

¹ School of Atmospheric Physics, Nanjing University of Information Science and Technology, Nanjing 210044, China

² College of Safety Science and Engineering, Nanjing Tech University, Nanjing 211816, China

³ Institute of Heavy Rain, CMA, Wuhan 430205, China

⁴ Reading Academy, Nanjing University of Information Science and Technology, Nanjing 210044, China

* Correspondence: niusj@njtech.edu.cn; Tel.: +86-139-1395-0111

Abstract: The precipitation and raindrop size distribution (RSD) characteristics of the four seasons and different rain types were studied using a PARSIVEL² raindrop disdrometer set in the southwest mountain areas of China from 2019 to 2021. The seasonal precipitation in the southwest mountain areas was mainly stratiform rain. The peaks of the RSD were about 1–2 orders of magnitude higher than those in the plains. The convective rain in spring and autumn was very close to the ocean-like convective mass. The local shape–slope (μ – Λ), radar reflectivity–rain rate (Z – R), and kinetic energy–rain rate (KE – R) relationships were further derived, and the diversity of these relationships was mainly due to the variability of the RSDs. In addition, the differences in the RSD characteristics between the top and the foot of the mountain during a typical precipitation process in the summer of 2020 were further compared. It was found that the number density of the small particles at the top of the mountain was higher than that at the foot of the mountain due to the broken large raindrops caused by the high wind speed, while the high evaporation rate, strong convective available potential energy (CPAE), and water vapor content at the foot of the mountain could strengthen the RSD, making the number density of the large raindrops at the foot of the mountain higher than that at the top.

Keywords: southwest mountain areas; raindrop size distribution (RSD); seasonal variation; rain types; different heights



Citation: Wu, H.; Niu, S.; Zhou, Y.; Sun, J.; Lv, J.; He, Y. Characteristics of Raindrop Size Distributions in the Southwest Mountain Areas of China According to Seasonal Variation and Rain Types. *Remote Sens.* **2023**, *15*, 1246. <https://doi.org/10.3390/rs15051246>

Academic Editor: Christopher Kidd

Received: 17 January 2023

Revised: 21 February 2023

Accepted: 22 February 2023

Published: 24 February 2023



Copyright: © 2023 by the authors. Licensee MDPI, Basel, Switzerland. This article is an open access article distributed under the terms and conditions of the Creative Commons Attribution (CC BY) license (<https://creativecommons.org/licenses/by/4.0/>).

1. Introduction

Raindrop size distribution (RSD) reflects the variation in raindrop density with respect to raindrop size. Studying RSD characteristics can enhance the understanding of the cloud microphysical processes in precipitation systems [1]. It is of great importance for the exploration of intra-cloud rain formation mechanisms [2], the improvement and revision of the cloud microphysical parameterization schemes in numerical models [3], and improving the accuracy of quantitative radar precipitation estimations [4].

RSD characteristics are closely related to rain types. Understanding the RSD characteristics of different rain types is helpful for understanding various cloud-related processes [5]. Different rain types (stratiform rain and convective rain) originate from different precipitation cloud systems. The two types can occur independently or simultaneously, and when they occur simultaneously, they are called mixed rain [6]. The observation results of RSD are used to analyze different rain types [7–9]. It has been found that the number of small raindrops in stratiform rain is concentrated and that the spectral shape is steep, while the number density of large raindrops in mixed rain and convective rain is high and the spectral shape is wide.

Previous studies have also shown that RSDs not only exhibit different characteristics depending on precipitation type but also vary according to climate characteristics and geographical location. In addition, many other studies have revealed seasonal and diurnal variations in RSDs. Zeng et al. (2019) analyzed the variation in RSDs in South China before and after the onset of a monsoon in the South China Sea and found that monsoon precipitation was dominated by small raindrops but that the concentration of medium raindrops was higher than that of pre-monsoon and post-monsoon precipitation [10]. Tang et al. (2014) compared the RSDs in Beijing, Zhangbei (North China), and Yangjiang (North China) and found that there are significant regional differences in the rainfall microphysical parameters of convective rain and small regional differences in the rainfall microphysical parameters of stratiform rain [11]. Wen et al. (2019) compared the RSDs of the four seasons in Nanjing and found that the raindrop size and raindrop concentration were largest in summer. The number concentration of small raindrops in autumn was slightly lower than that in summer, but the maximum diameter of the raindrops in the two seasons was similar [12]. Chen et al. (2013) analyzed the characteristics of the RSD in Naqu in the Qinghai–Tibet Plateau and the influence of diurnal variation and found that the mass-weighted mean diameter (D_m) of the convective rain in the daytime was larger than that at night, while the logarithm of the generalized intercept parameter ($\log_{10}N_w$) was smaller than that at night [13].

In the past, statistical studies on the regional characteristics of RSDs mainly focused on plains and hills [14–18], and some focused on the plateau [19,20]. There are few analyses of the variation characteristics of the RSDs in mountain areas. The Wuling Mountains are located in the southwest mountain areas of China, which is the eastern extension of the Yunnan–Guizhou Plateau. They have an average elevation of over 1000 m, 70% of which is more than 800 m above the sea. With unique mountain climatic characteristics and complex topography and substratum coupled with the influence of the monsoon climate, the weather changes drastically and is accompanied by many disasters. Low temperatures and cloudy rain, heavy rain, short-time heavy precipitation, and freezing rain are all common catastrophic weather in the Wuling Mountains. Moreover, as far as we know, due to the lack of long-term continuous RSD measurements, the seasonal variations in their RSDs have been subjected to limited investigations in China and remain unknown. Therefore, this paper investigated the discrepancies in their RSDs using the disdrometer data obtained in the Wuling Mountains from 2019 to 2021. The RSD characteristics were studied under four seasons and three rain types and were compared at different heights. The main microphysical process of precipitation among the different heights was analyzed as well. This study is organized as follows: The data and methodology are introduced in Section 2. The characteristics of the RSDs in the study region and the results of the RSD features of the rainfall at the top and foot stations are given in Section 3 followed by a discussion in Section 4, and the conclusions are presented in Section 5.

2. Data and Methods

2.1. Observation Sites and Instruments

The observation sites were located at Enshi Weather Radar Station (30.28°N, 109.27°E, altitude of 1722 m) and Xianfeng Meteorological Bureau (29.68°N, 109.14°E, altitude of 778 m) in the north part of Wuling Mountains as shown in Figure 1. The observation time was from 16 November 2019 to 12 December 2021.

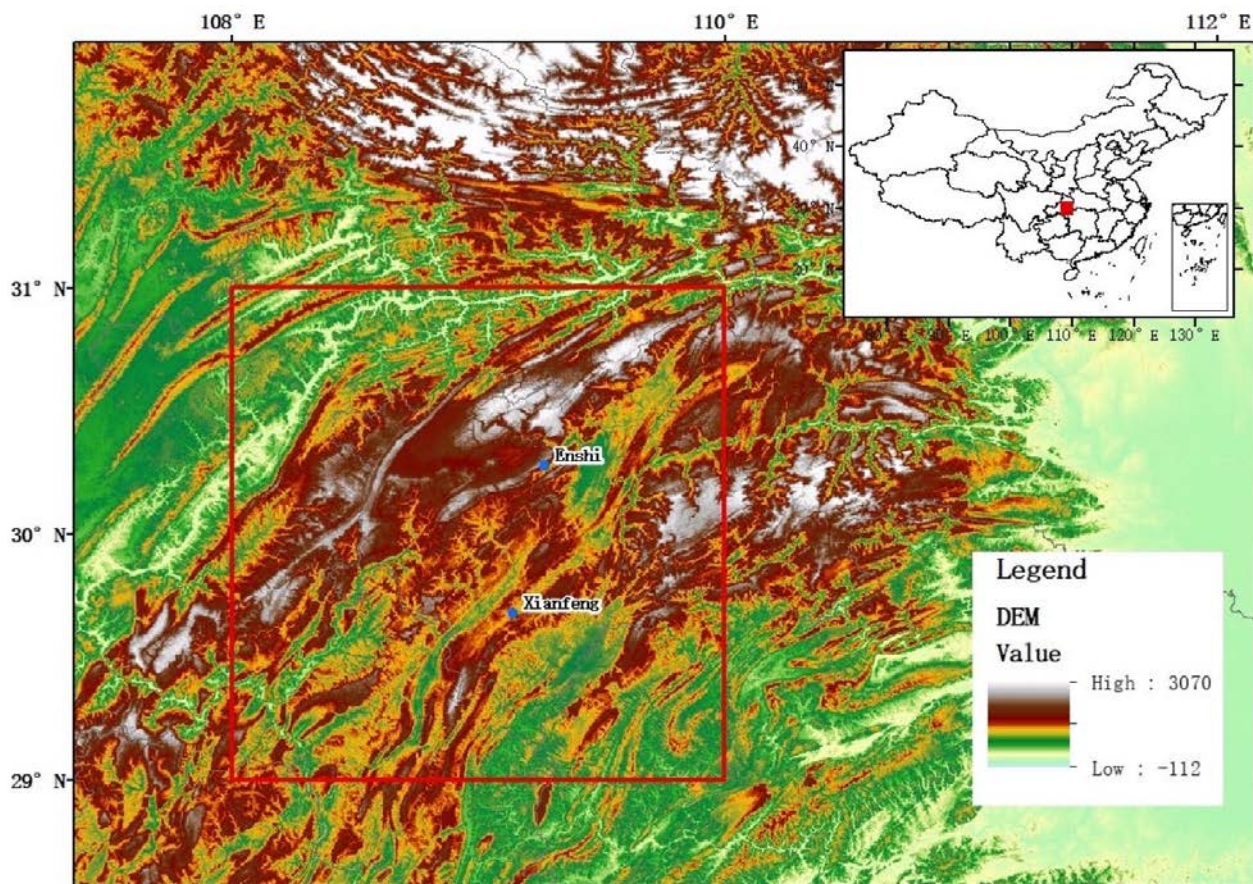


Figure 1. Location of Enshi Weather Radar Station and Xianfeng Meteorological Bureau in the Wuling Mountains (red box) with shading representing the topography (m). A snapshot of the location of Wuling Mountains in China is shown in the upper right corner.

A PARSIVEL² raindrop disdrometer was used, which uses a laser system to measure the falling speed and diameter of precipitation particles. The PARSIVEL² automatic precipitation laser particle spectrometer is an optical particle spectrometer produced by OTT (Germany) which can be used for the measurement of solid particles (snow, graupel, hail) [21,22]. PARSIVEL² has 32 particle size channels and 32 velocity channels; the particle size ranges from 0 to 25 mm, and the velocity ranges from 0 to 22.4 m s⁻¹. The time resolution is 1 min. Wen (2016) compared the minute precipitation rate of PARSIVEL² with that of 2DVD (Two-Dimensional Video Disdrometer) and MMR (Micro Rain Radar) and found that the correlation coefficients were all over 0.95 [23]. Before observation, the rainfall amounts observed with Parsivel² were compared with the surface rain gauge and 2DVD to verify the accuracy of it, and the correlation between them was over 0.95 [24]. It was ensured that the firmware versions of Parsivel² in Enshi and Xianfeng are the same.

In addition, the temperature, specific humidity, CAPE, and water vapor content of the whole layer used to describe the climatological background were provided by ERA5 reanalysis datasets with a time resolution of 1 h and a spatial resolution of 0.25° × 0.25°. Specifically, in this study, March, April, and May were divided into spring; June, July, and August were summer; September, October, and November were autumn; and December, January, and February were winter.

2.2. Quality Control and Data Processing

Before data processing, the quality of RSD data was controlled as follows: (1) Due to the low signal-to-noise ratio, the first two size classes of data were eliminated [25]. (2) The data were removed when the temperature was <0 °C; then, according to the theoretical

formula of the final falling velocity of raindrops proposed by Gunn et al. (1994) [26] and various empirical formulas of the final falling velocity of solid precipitation particles of different forms proposed by Locatelli et al. (1974) [27], the data near the theoretical formula of the final falling velocity of raindrops were retained, and the data within the range of the final falling velocity of solid precipitation particles were excluded. Since the Enshi Weather Radar Station is at an altitude of 1722 m with an air pressure of 812 hpa, it was necessary to correct the air density for the final falling velocity of solid and liquid particles. The corrected coefficient adopted was $\left(\frac{\rho_0}{\rho}\right)^{0.5}$, where ρ is the actual air density and where ρ_0 is the standard atmospheric air density [28]. (3) The 1 min samples with counts of raindrops of <5 or rain rates of $<0.01 \text{ mm h}^{-1}$ were discarded, and (4) data with raindrop diameters greater than 6 mm were excluded because raindrops larger than 6 mm in diameter are rare in natural rainfall and often break up on their way to the ground. After this series of quality control, a total of 112,082 min of valid data was obtained. The distribution of mean concentration (color bar) of RSDs with diameter and velocity after quality control is shown in Figure 2, and the equation for final falling velocity with diameter of different particles is shown in Table 1.

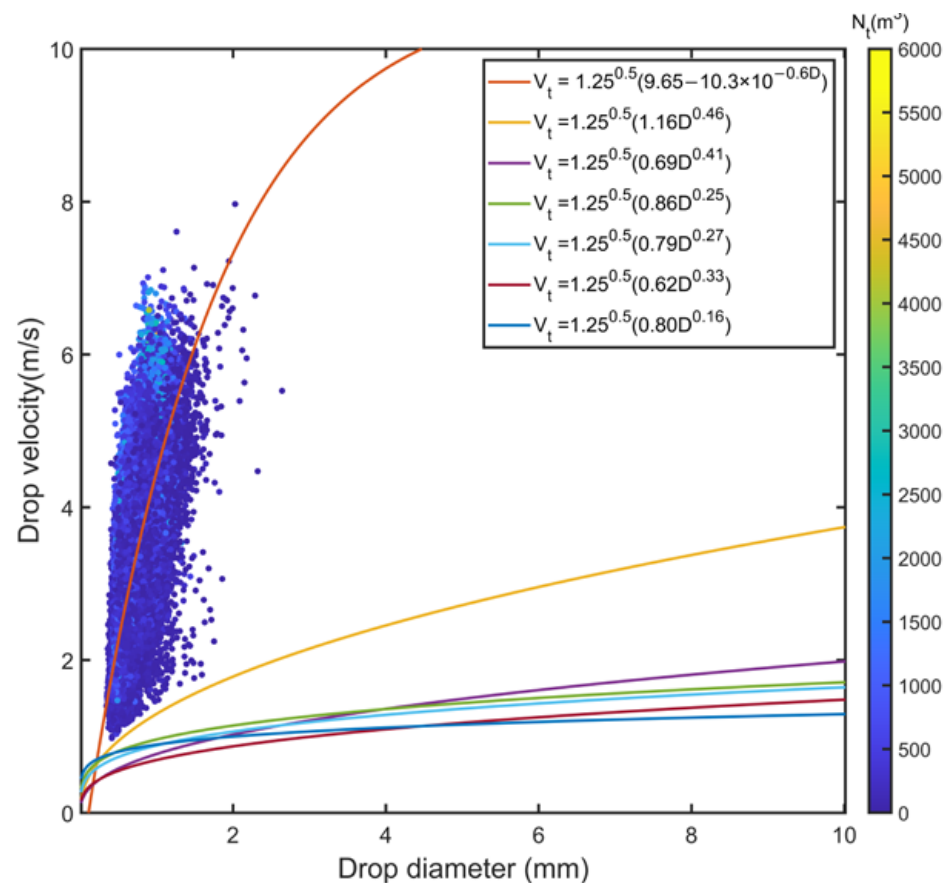


Figure 2. Distribution of mean concentration (color bar) of RSD with diameter and velocity after quality control.

Table 1. Equation for final falling velocity with diameter of different particles.

Hydrometer Types	Terminal Velocity
Raindrop	$V_t = 1.250.5 (9.65 - 10.3 \times 10^{-0.6D})$
Graupel	$V_t = 1.250.5 (1.3D^{0.66})$
Aggregates of unrimed radiating assemblages of plants, bullets, and columns	$V_t = 1.250.5 (0.69D^{0.41})$
Graupel-like snow of hexagonal type	$V_t = 1.250.5 (0.86D^{0.25})$
Aggregates of densely rimed radiating assemblages of dendrites	$V_t = 1.250.5 (0.79D^{0.27})$
Densely rimed dendrites	$V_t = 1.250.5 (0.62D^{0.33})$
Aggregates of unrimed radiating assemblages of dendrites	$V_t = 1.250.5 (0.8D^{0.16})$

Using the RSD data after quality control, the number concentration of raindrops N (D_i) ($\text{mm}^{-1} \text{m}^{-3}$), radar reflectance factor Z ($\text{mm}^6 \text{m}^{-3}$), rain rate R (mm h^{-1}), and other microphysical quantities could be calculated. The above relevant calculation methods can be referred to previous studies [15,29]. In the study, the three control parameters (μ , Λ , and N_0) of gamma RSD model [30] were obtained by measuring the second, fourth, and sixth moments of RSDs using the moment truncation fitting method (TMF) proposed by Vivekanandan et al. (2014) [31].

2.3. Classification of Rain Types

In this study, rain types were classified as stratiform rain, mixed rain, and convective rain. According to the relationship between the generalized intercept parameter N_w ($\text{m}^{-3} \text{mm}^{-1}$) and the median volume diameter D_0 (mm), stratiform rain and convective rain were distinguished by Bringi et al. (2009) [32]. Thurai et al. (2016) introduced the likelihood index i to divide the rain types into stratiform, mixed, and convective [9]. In this paper, rain types were divided according to their method, and the formula used is as follows:

$$i = \log_{10} N_w - \log_{10} N_w^{sep} \quad (1)$$

N_w^{sep} is N_w on the line separating convective and stratiform data points on D_0 - $\log_{10} N_w$ plane given by

$$\log_{10} N_w^{sep} = -1.6D_0 + 6.3 \quad (2)$$

For the gamma distribution, D_0 could be represented by D_m , $D_0 = \frac{(3.67+\mu)}{(4+\mu)} D_m$, and D_m was a reasonable approximation of D_0 for all $\mu > -2$ [30]. $i \leq -0.3$ was classified as stratiform rain, $0.3 < i < 0.3$ was classified as mixed rain, and $i > 0.3$ was classified as convective rain. After classification using this method, over 112,082 min of effective precipitation, stratiform rain occurred for 103,435 min, mixed rain occurred for 6851 min, and convective rain occurred for 1796 min.

2.4. Climatological Backgrounds

Figure 3 shows the seasonal averages of reanalyzed wind field and relative humidity at 850 hPa. As shown in Figure 3, Enshi and Xianfeng were humid all year round, with the relative humidity reaching about 90% in each season. They had a typical subtropical monsoon climate. In summer, sufficient warm and moist air was transported from the Indian Ocean and the South China Sea to the southwest mountain areas by the dominant southwest winds [33], which, coupled with the uplifting effect of the Wuling Mountains, led to increased convective instability in the region and made it prone to heavy precipitation. Additionally, in autumn and winter, convection was usually weaker as the summer monsoon weakened and as weak cold air from the northwest invaded.

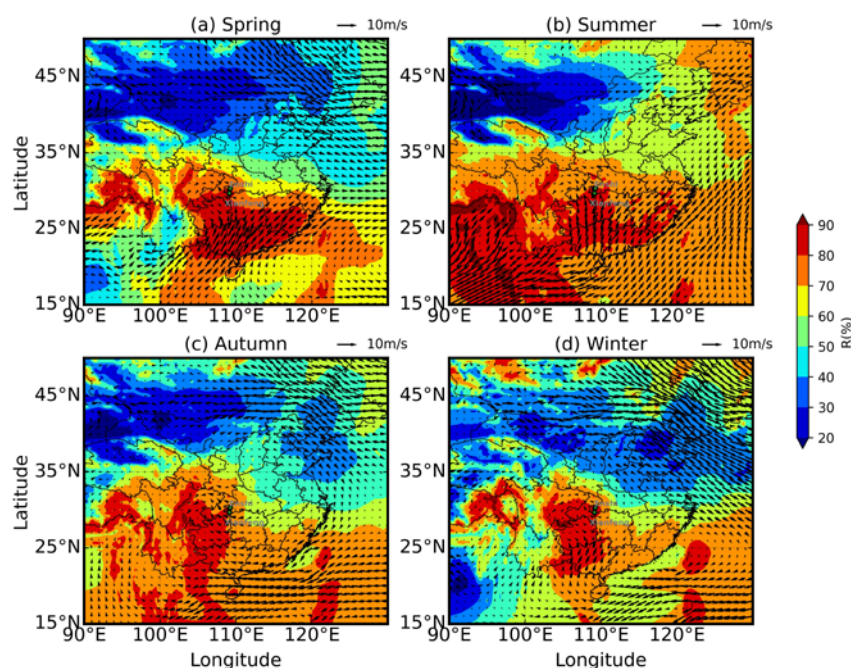


Figure 3. Seasonal mean wind field (10 m s^{-1}) and relative humidity (%) at 850 hPa based on the ERA5 from 2019 to 2021.

2.5. Precipitation Duration and Rainfall Contribution

The precipitation duration of the different rain types during different seasons are listed in Table 2. As revealed from Table 2, the proportion of stratiform rain in the total precipitation duration was very high, reaching 92.3%. In terms of seasons, the precipitation duration was the longest in summer, accounting for 36.4%, followed by autumn, accounting for 32.2%; spring, accounting for 24.6%; and winter, accounting for 6.8%. This was different from the fact that the precipitation duration in southeast mountain areas of China was summer, spring, winter, and autumn in descending order [34].

Table 2. The precipitation duration for the different rain types during different seasons.

Season	Rain Type	Duration	The Total Duration of the Season
Spring	Stratiform	26,050 min	27,491 min
	Mixed	1078 min	
	Convective	363 min	
Summer	Stratiform	35,440 min	40,814 min
	Mixed	4325 min	
	Convective	1049 min	
Autumn	Stratiform	34,879 min	36,115 min
	Mixed	1017 min	
	Convective	219 min	
Winter	Stratiform	7066 min	7662 min
	Mixed	431 min	
	Convective	165 min	

Figure 4 shows the percentage occurrence of different rain types and their contributions to rainfall amount during different seasons. There were slight differences in the incidence of rain types in the four seasons. There were 94.8%, 86.8%, 96.6%, and 92.2% chances that stratiform rain would occur in spring, summer, autumn, and winter during the 2-year period; mixed rain's chances were 3.9%, 10.6%, 2.8%, and 5.6%; and convective rain's chances were 1.3%, 2.6%, 0.6%, 2.2%, respectively. When considering the contribution to

rainfall, other than winter being dominated by stratiform rain (62.9%), in the other three seasons, the total contribution of stratiform rain and convective rain was more than 80%.

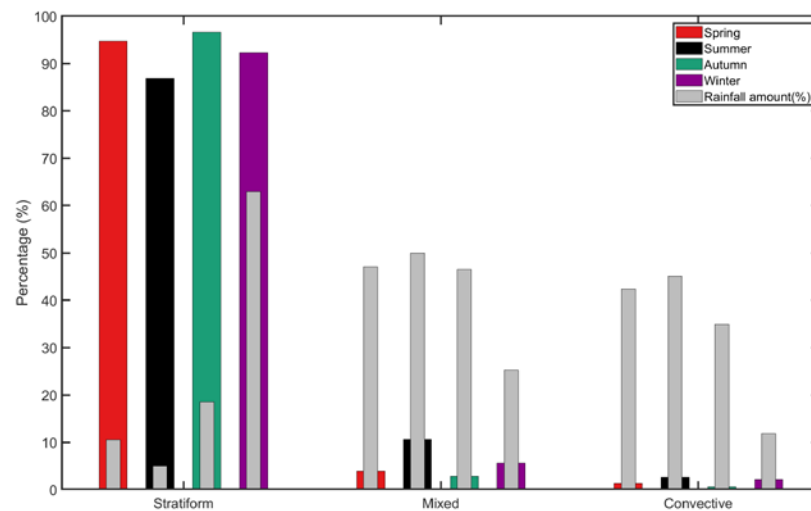


Figure 4. Percentage occurrence and contribution to rainfall amount of different rain types during different seasons.

3. Results

3.1. Microphysical Parameter Characteristics

Table 3 shows the mean values of the parameters of the different rain types in the four seasons. For all the rain types (stratiform rain, mixed rain, and convective rain), the mean values of LWC , R , D_m , and Z gradually increased. The D_m of convective rain was three times greater than the D_m of stratiform rain. However, the mean of N_t and $\log_{10}N_w$ was largest for mixed rain. From the perspective of seasonal variation, the relatively large raindrop diameter and the high concentration of the raindrops in summer made the highest R among the four seasons, while the R values of spring, autumn, and winter were similar.

Table 3. Mean values of the total raindrop concentration N_t (m^{-3}), liquid water content LWC ($g m^{-3}$), rain rate R ($mm h^{-1}$), mass-weighted mean diameter D_m (mm), logarithm of generalized intercept parameter $\log_{10}N_w$ ($mm^{-3} m^{-1}$), and radar reflectivity Z (dBZ).

Rain Type	Season	Samples (min)	N_t (m^{-3})	LWC ($g m^{-3}$)	R ($mm h^{-1}$)	D_m (mm)	$\log_{10}N_w$ ($m^{-3} mm^{-1}$)	Z (dBZ)
Stratiform	Spring	26,050	250	0.05	0.66	0.87	3.72	15.47
	Summer	35,440	345	0.07	0.87	0.86	3.86	16.65
	Autumn	34,879	351	0.06	0.65	0.79	3.91	14.83
	Winter	7066	336	0.07	0.71	0.91	3.81	18.03
Mixed	Spring	1078	886	0.46	7.19	1.56	3.85	35.27
	Summer	4325	1247	0.48	7.15	1.24	4.28	32.34
	Autumn	1017	1349	0.40	5.64	1.18	4.34	30.53
	Winter	431	805	0.36	4.67	1.64	3.71	34.50
Convective	Spring	363	745	0.98	19.20	2.68	3.16	45.82
	Summer	1049	1193	1.37	26.58	2.28	3.63	45.01
	Autumn	219	900	1.03	19.64	2.79	3.10	45.67
	Winter	165	218	0.43	5.74	3.33	2.41	45.35
All	Spring	27,491	282	0.08	1.16	0.92	3.72	16.65
	Summer	40,814	462	0.15	2.20	0.94	3.90	19.04
	Autumn	36,115	383	0.07	0.91	0.82	3.91	15.46
	Winter	7662	360	0.09	1.04	1.01	3.78	19.55

3.2. Characteristics of RSD

Figure 5 shows the composite raindrop spectra of the different rain types in the different seasons. The RSDs of stratiform rain and mixed rain both show their unimodal distribution in the different seasons, while the RSDs of convective rain show a multi-peak structure. The reason for this phenomenon is that the formation mechanism of stratiform rain is different from that of convective: the sizes of the raindrop particles in stratiform rain are similar, and the interactions of the raindrop particles are small; therefore, the volume of the raindrops will not increase obviously, while, when convection is strong, the strong upward motion leads to the intensification of the collision process. The average size of the raindrops of convective rain was larger than that of stratiform rain, and the multi-peak structure was more likely to appear. Moreover, the peak value of convective rain was about one order of magnitude higher than that of stratiform rain in spring, summer, and autumn but about one order of magnitude lower in winter. This was because the updraft in convective rain was larger, the crushing process was important, and the rainfall particles with small diameters and that were of a greater number were easy to form near the ground. The CAPE and the amount of moisture are two important factors usually used to determine the formation and growth of convection [35]. The CAPE and water vapor for the four seasons are presented in Figure 6. As can be seen, the CAPE and water vapor during summer were highest, which suggests that precipitation was more intense during this period. Winter was dominated by stable stratiform rain, and, under the control of dry and cold air, the convective system was dominated by shallow and weak convection in winter.

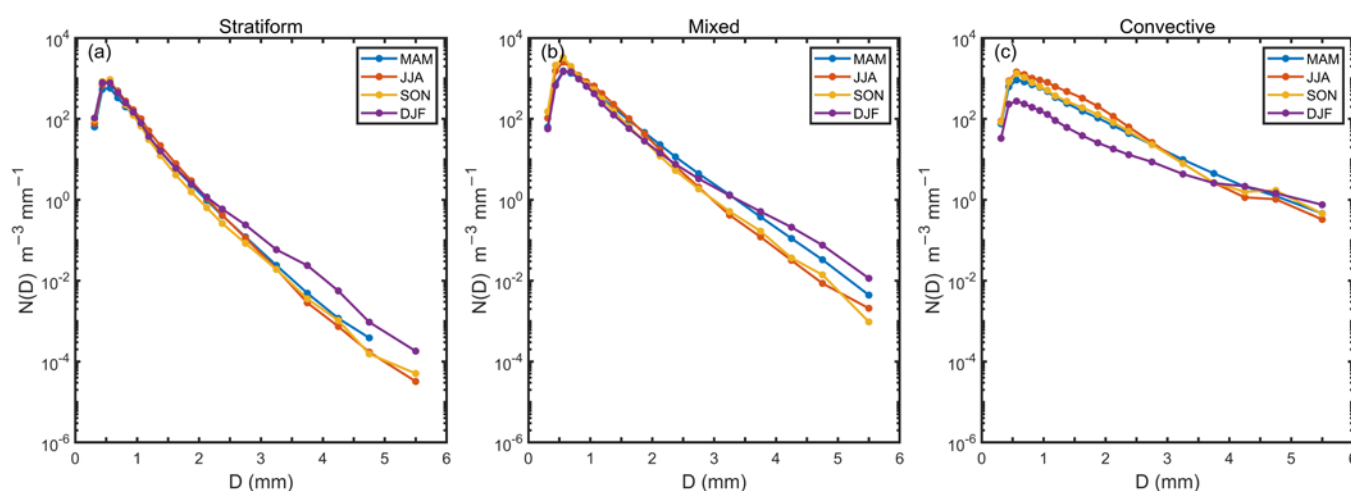


Figure 5. Composite raindrop spectra of stratiform rain (a), mixed rain (b) and convective rain (c) in different seasons.

Table 4 shows the RSD peak number densities of the different rain types in different regions. As can be seen from Table 3, the RSD in Enshi was the same as that in Huangshan [36] and Lushan [37], and their peaks were one order of magnitude higher than those of the plains [15,28,38]. This may be because wind shear, gravity sorting, evaporation, collision and fragmentation, and other factors affected the RSD characteristics. Compared with plain precipitation, mountain precipitation was more likely to occur in the cloud with smaller effect of evaporation, and there were more small particles under cloud observation. Meanwhile, the turbulence and collision in the cloud were likely to cause the droplets to break up and form small droplets, so the RSD in Enshi had the characteristics of topographic rain [39].

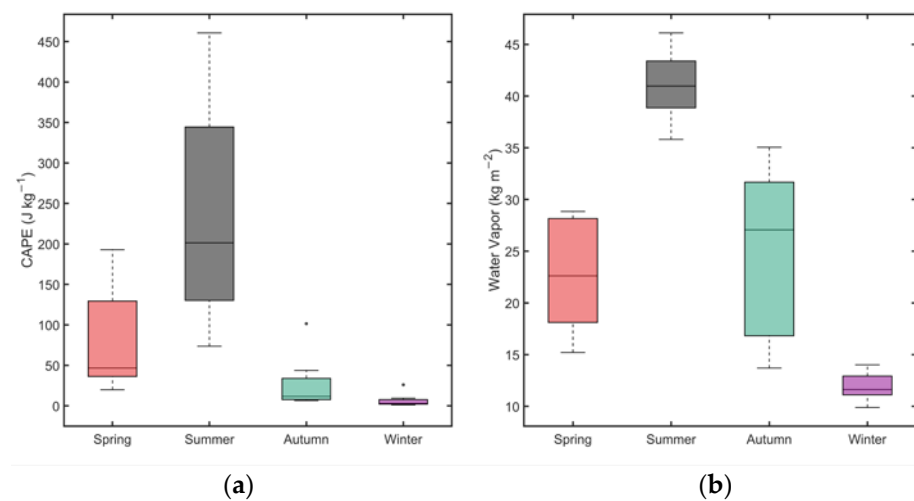


Figure 6. CAPE (a) and water vapor (b) in southwest mountain areas for the four seasons.

Table 4. RSD peak number density of different rain types in different regions [15,28,36–38].

Region	Stratiform	Mixed	Convective
This study	10^3	10^3	10^3
Mt. Huang [36]	10^3	-	10^3
Mt. Lu Shang [37]	10^3	10^4	10^4
Liao Ning [38]	48	48	46
Nang Jing [15]	10^2	-	10^2
Gu Yuan [28]	10^2	-	10^2

3.3. Distribution of D_m and $\log_{10}N_w$

Figure 7 shows the cumulative distribution functions (CDFs) of R , D_m , and $\log_{10}N_w$ with respect to population and rainfall contributions of the different seasons and rain types. In terms of season, in spring, autumn, and winter, precipitation under 8 mm h^{-1} all showed a nearly 100% population and contributed 65%, 80%, and 85% to the rainfall amount, respectively. The difference between them was that only 5% precipitation was higher than 8 mm h^{-1} in summer, but it still contributed up to 50% to the rainfall amount. D_m and $\log_{10}N_w$ also showed obvious seasonal variations. More than 80% of D_m was less than 1.3 mm in all four seasons, but their contributions to the rainfall amount varied widely from 38% in winter to 65% in autumn. In addition, the CDF of D_m in winter was always lower than those in the other three seasons; this indicates that the probability of larger raindrops was higher in winter. The population and rainfall contribution curves were similar between summer and autumn; they almost coincided in some intervals and differed by no more than 0.2. When $\log_{10}N_w$ was $< 3.8 \text{ mm}^{-3} \text{ m}^{-1}$, it contributed to the greatest rainfall amount in winter, while, when $\log_{10}N_w$ was $> 3.8 \text{ mm}^{-3} \text{ m}^{-1}$, it contributed to the lowest rainfall amount in spring. Out of the different rain types, the two CDF curves of R , D_m , and $\log_{10}N_w$ of stratiform rain and mixed rain changed synchronously, while those of convective rain was quite different. For convective rain, precipitation higher than 25 mm h^{-1} , which contained a population of 40%, still contributed 70% to the rainfall amount. Nearly 80% and 60% of D_m and $\log_{10}N_w$ contributed about 60% and 40% to the rainfall amount.

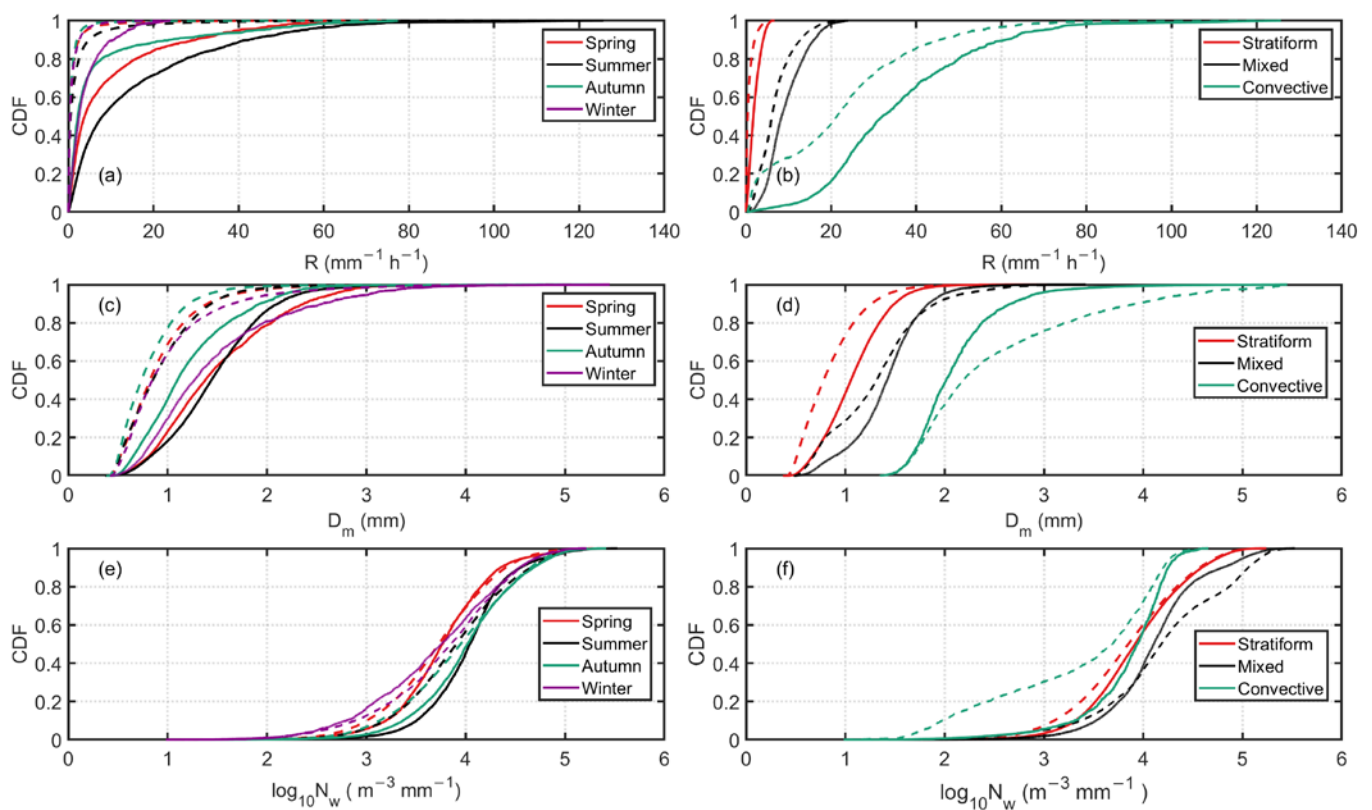


Figure 7. CDF of population (dashed lines) and rainfall contribution (solid lines) of R , D_m , and $\log_{10}N_w$ during different seasons (a,c,e) and of different rain types (b,d,f).

The RSD in the southwest mountain areas was compared with the results of Bringi et al. (2003) [8] in other regions. Figure 8a shows the mean of the $\log_{10}N_w$ and D_m of stratiform rain, mixed rain, and convective rain. Superimposed on the scatter plot are two rectangles corresponding to the ocean-like and continental-like convective clusters as defined by Bringi et al. (2003) [8]. It can be seen that the stratiform rain in each season was concentrated in the area of $\log_{10}N_w$ from 3.72 to 3.91 $\text{mm}^{-3} \text{m}^{-1}$ and in the area of D_m from 0.79 to 0.92 mm. However, the seasonal differences between mixed rain and convective rain were obvious, and the $\log_{10}N_w$ and D_m values of mixed rain in summer were close to those in autumn; the same case occurred in spring and winter. Convective rain was different in other seasons except for the $\log_{10}N_w$ and D_m values in spring and autumn. The convective rain in spring and autumn was very close to the oceanic convective mass. The D_m of the convective rain in summer was similar to that of ocean-like convective rain, but $\log_{10}N_w$ was about 0.2 $\text{mm}^{-3} \text{m}^{-1}$ higher than that of ocean-like convective rain. The D_m and $\log_{10}N_w$ of the convective rain in winter were quite different from those of continental- and ocean-like convective rain. Compared with Nanjing [12] and Naqu [13], the D_m and $\log_{10}N_w$ of stratiform rain and mixed rain in Enshi were relatively close to those in Seoul, but the convective rain had a larger D_m and smaller $\log_{10}N_w$. In addition, unlike the stratiform rain and convective rain in Nanjing, where there was little season variation in D_m and $\log_{10}N_w$, the D_m and $\log_{10}N_w$ of convective rain varied considerably between the seasons in the southwest mountain areas. It was also noted that the stratiform rain in winter had a relatively low $\log_{10}N_w$ and high D_m , while the convective rain had a relatively high $\log_{10}N_w$ and low D_m , which corresponded to the N0 jump effect mentioned in [40]. In a large range of rainfall, there is a sudden change in RSD, which often means a shift in the mesoscale weather region, and this situation can be identified by a sudden change in N0. In view of a microphysical point, a smaller number of large dry snowflakes melting near the zero-degree layer leads to a small $\log_{10}N_w$ and large D_m . At this point, the bright band of the zero-degree layer is strong. However, when the small ice particles melt, a large $\log_{10}N_w$ and small D_m will be

generated, and the bright band of the zero-degree layer will be weak. The N0 jump effect occurs when $\log_{10}N_w$ and D_m are converted [8].

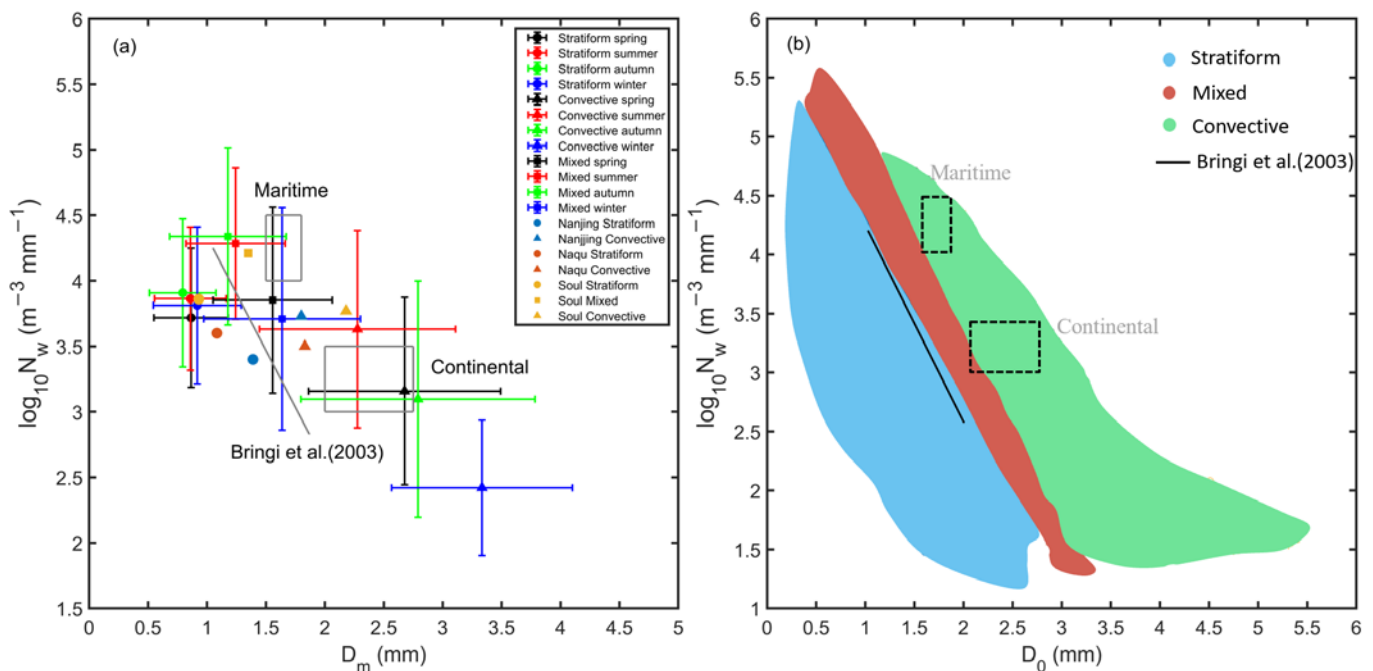


Figure 8. The average value of $\log_{10}N_w$ versus average D_m for undefined rain, stratiform rain, mixed rain, and convective rain with their respective standard deviations ($\pm 1 \sigma$). The points below the dotted line represent stratiform rain, while the points above the line represent convective rain. The outlined rectangles correspond to the maritime and continental convective clusters reported by Bringi et al. (2003) [8] (a). D_0 - $\log_{10}N_w$ distribution conceptual model with reference (Figure 12) to Dolan et al. (2008) [41] (b).

In order to study the possible mechanism of RSD formation in the southwest mountain areas, the D_0 - $\log_{10}N_w$ conceptual model in Figure 8b was plotted. With reference to the conclusion reached by Dolan et al. (2008) [41], Figure 8b shows that the mechanisms of the convective rain in the southwest mountain areas could be roughly divided into two types. The first type is convective rain dominated by ice phase particles, which is characterized by a large D_0 and a low $\log_{10}N_w$. This is because strong vertical motion supports the generation and development of graupel and hail particles, resulting in a number of raindrops falling to the ground under the action of the melting process. The second type is mainly related to the “warm rain growth—ice phase process”. The stratiform rain could be divided into three types. The first has a number of small raindrops with low ETH and usually has weak reflectance, corresponding to warm showers. In the tropics, this type is associated with weak convective motion, but, in topographic forcing locations such as OLYMPEX, Dolan et al. (2018) pointed out that this may be a sign of enhanced topography. The other two are aggregation—riming processes, where D_0 increases and $\log_{10}N_w$ decreases [41].

3.4. μ - Λ Relationship

Gamma distribution functions have been widely used in microphysical parameterization schemes to describe different RSD characteristics. The shape parameter μ is usually kept constant, while the other two parameters Λ and N_0 are usually treated as predictor variables. Such microphysical schemes are often called second-moment schemes. Milbrandt et al. (2005) found that, for second-moment schemes with a fixed μ , the microphysical properties of clouds and precipitation are sensitive to the μ values because shape parameters play an important role in determining sedimentation and microphysical growth rates [42]. Considering that the three parameters of the gamma distribution are not indepen-

dent of each other, Zhang et al. (2001) proposed an empirical relationship between μ and Λ to test the gamma distribution. That is, when R is $>5 \text{ mm h}^{-1}$ and when the number of raindrops is >1000 , the μ - Λ relation is $\Lambda = 0.0365 \mu^2 + 0.735 \mu + 1.935$, which is suitable for a Λ between 0 and 20 mm [43]. Although this relationship was derived from the observations of meteoric precipitation over Florida, Thurai et al. (2010) found that the relationship was also suitable for Oklahoma [44]. However, Zhang et al. (2003) also pointed out that the μ - Λ relationship may vary with climate and rain types [45]. The adjusted μ - Λ relationship should be derived from local RSD observations for an accurate precipitation RSD estimation. Although the RSDs of all types of precipitation may exhibit a correlation between μ and Λ , it is important to analyze the RSDs collected in different geographical locations and different seasons to understand the variability of the μ - Λ relationship. [15,31,46,47].

In this study, considering that the differences in the coefficients of the relationships for the four seasons in the southwest mountain areas were minor, the μ - Λ relations were derived for the three rain types following the same data procedure as in Zhang et al. (2003) [45]. Figure 9 shows the μ - Λ relationships for the different rain types, and it also shows the fitting curves of previous studies as well as the corresponding curves when $D_m = 0.5, 1.0, 2.0,$ and 3.0 mm ($\Lambda D_m = 4 + \mu$). As can be seen from Figure 9, the whole μ - Λ relationship in the southwest mountain areas was different from that obtained in Florida. Compared with our study, the Florida curve had higher coefficients, especially the square term. Given the same Λ value, the μ value of the Florida curve (the red dashed line) was lower than that of our fit (the purplish-red solid line). The distance between the two curves increased with an increase in the Λ value. This difference was mainly related to the feature size parameters. Ulbrich (1983) insisted that, for gamma RSD, the μ - Λ relationship can be expressed as $\Lambda D_m = 4 + \mu$ [30]. Therefore, given the D_m and μ values, the corresponding Λ value can be estimated. As shown in Figure 9, the fit of the southwest mountain areas appeared in the higher D_m region compared to the Florida curve, indicating that its RSDs had higher D_m values than those observed in Florida. In other words, given the same Λ value, the higher D_m value may be responsible for the higher μ value than that in Florida. This supports the agreements that μ - Λ relationship varies with geographical location because each location has different RSD characteristics [41,45]. Moreover, the fit of the convective rain in the southwest mountain areas was consistent with the observation of the Meiyu season in Nanjing and the observation during the tropical cyclones in the Northern Indian Ocean, while the fits of all and mixed rain were consistent with the observation in summer over the Western Tianshan Mountains. Another interesting finding was that, for a given Λ , the μ obtained with JWD and PARSIVEL was much greater than the μ obtained with 2DVD. This occurred because JWD and PARSIVEL generally underestimate small raindrops and overestimate large raindrops, which changes the RSD and produces larger μ values, whereas 2DVD is more accurate at observing small drops, resulting in relatively smaller μ values. This also indicates that the μ - Λ relationships obtained by different instruments are quite different.

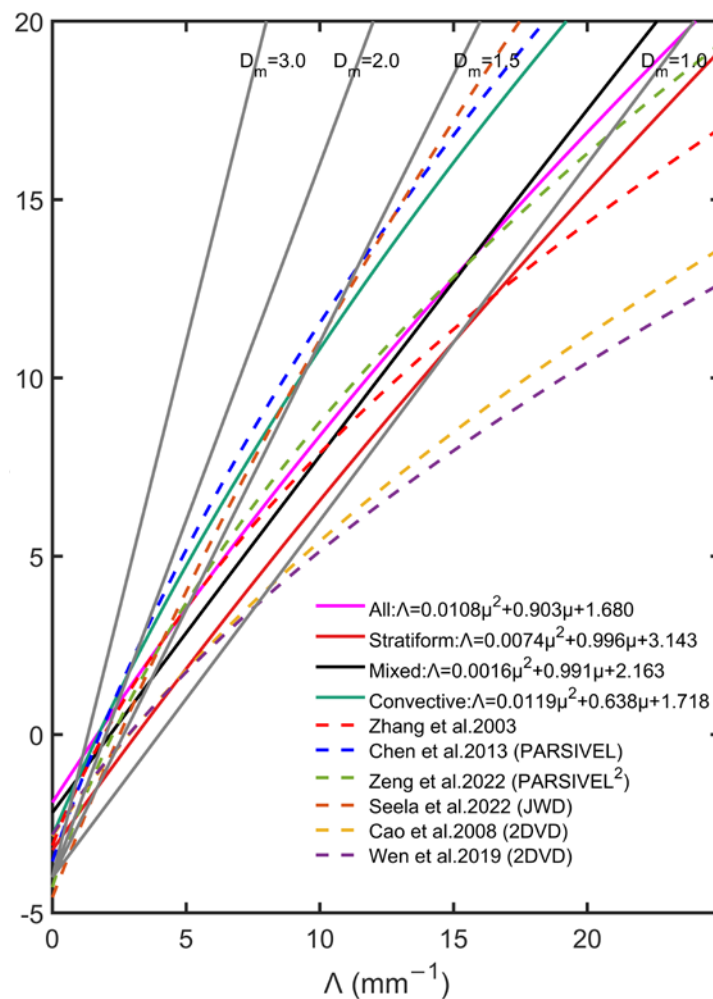


Figure 9. μ – Λ relationship of different rain types. The dashed lines represent the fitting of the μ – Λ relationship and the empirical μ – Λ relationship from Zhang et al. (2003) [45], Chen et al. (2013) [15], Zeng et al. (2022) [48], Seela et al. (2022) [49], Cao et al. (2008) [50], and Wen et al. (2019) [12], respectively. The gray lines correspond to the relationship $\Lambda D_m = 4 + \mu$ given the value of $D_m = 1.0, 1.5, 2.0,$ and 3.0 mm.

3.5. Z–R Relationship

The Z–R relationship is the basis of the radar quantitative estimation of precipitation. Rosenfeld et al. (2003) found that coefficient a and index b vary with geographical location, atmospheric conditions, and rain type [1] and that there is a close relationship between RSD variability and a and b [51,52]. Therefore, it was necessary to study the Z–R relationship of precipitation in the southwest mountain areas to better understand the variability of the Z–R relationship and to further improve radar QPE. Figure 9 shows the Z–R relationship of the different rain types, and the coefficients and index values of the fitted power law equations are also provided. For reference, the standard Z–R relationship, which is widely used in operational weather radar rainfall estimations, is also superimposed, $Z = 300R^{1.4}$ [53], which is the default relation used in the U.S.’s next-generation weather radar (NEXRAD). It can be seen from Figure 10 that there were certain differences in the Z–R relationships and the standard relationships of the four seasons, and the biggest difference in the standard relationship appeared in winter. Although the rainfall rarely exceeded 5 mm h^{-1} in winter, its $Z = 1085R^{1.27}$ relationship had the highest coefficient and the lowest exponent value, and the curve was located on the upper left of the other relationships. Because the Z was more sensitive to D_m than to the raindrop concentration, for a given Z , the largest D_m in winter led to the smallest R . Similarly, for a given Z , the autumn rainfall had the largest R

because autumn D_m was the smallest, resulting in a $Z = 334.50R^{1.35}$ relationship with the lowest coefficient and a relatively large index value.

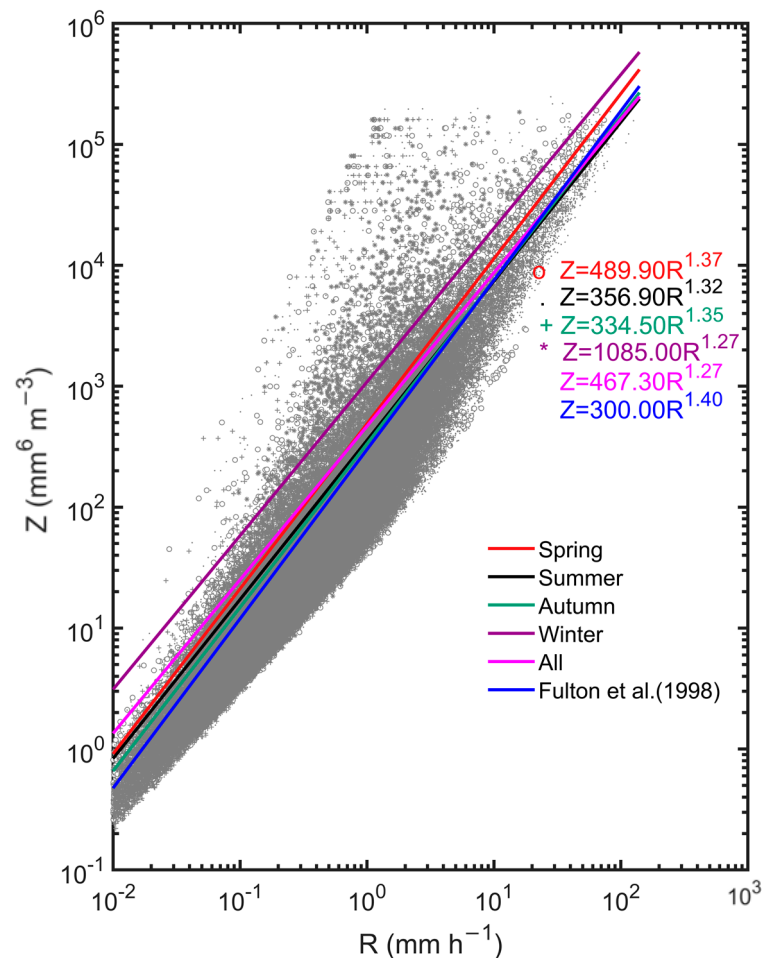


Figure 10. Z – R relationships and the fitted power law relations of the four seasons. The blue dashed line represents the standard NEXRAD Z – R relationship ($Z = 300R^{1.4}$, Fulton et al., 1998 [30]).

Using the common Z – R relationship $Z = 300R^{1.4}$ for comparison, convective rain had the problem of obviously underestimating precipitation [54]. Optimizing the Z – R relationship was particularly important to improve the ability to predict heavy rainfall. For an $R > 10 \text{ mm h}^{-1}$ (basically all convective rain), the lowest R was estimated for the given Z when the winter rainfall $Z = 1085R^{1.27}$ followed by the spring and autumn rainfall. Since the mean D_m in summer was relatively small and the N_t was the largest, the $Z = 356.90R^{1.32}$ relationship had the smallest exponent of the four relationships, which indicates that the R estimates of the same Z value were the highest during convective rainfall. The fitting $Z = 467.30R^{1.27}$ of all four seasons was consistent with the standard relationship on the whole.

Figure 11 shows the Z – R relationship of the different rain types. Considering that sporadic light rain was especially abundant in the southwest mountain areas, the Z – R relationship of different rain types was only studied when N_t was >1000 . As shown in Figure 11, coefficient a ranged from 65.87 to 484.20, and index b ranged from 1.25 to 2.05. Most of the points of stratiform rain and mixed rain were below the standard relationship, while the points of convective rain were more evenly distributed around the standard relationship. This indicates that the standard relationship used in the radar estimation of precipitation could partially overestimate stratiform rain and mixed rain in the southwest mountain areas, especially stratiform rain. In addition, the fitting relationship of each rain

type obtained by other scholars in Beijing, Xian, and Nanjing were also quite different from those in Enshi, which fully reflects the characteristics of the Z – R relationship changing with geographical location.

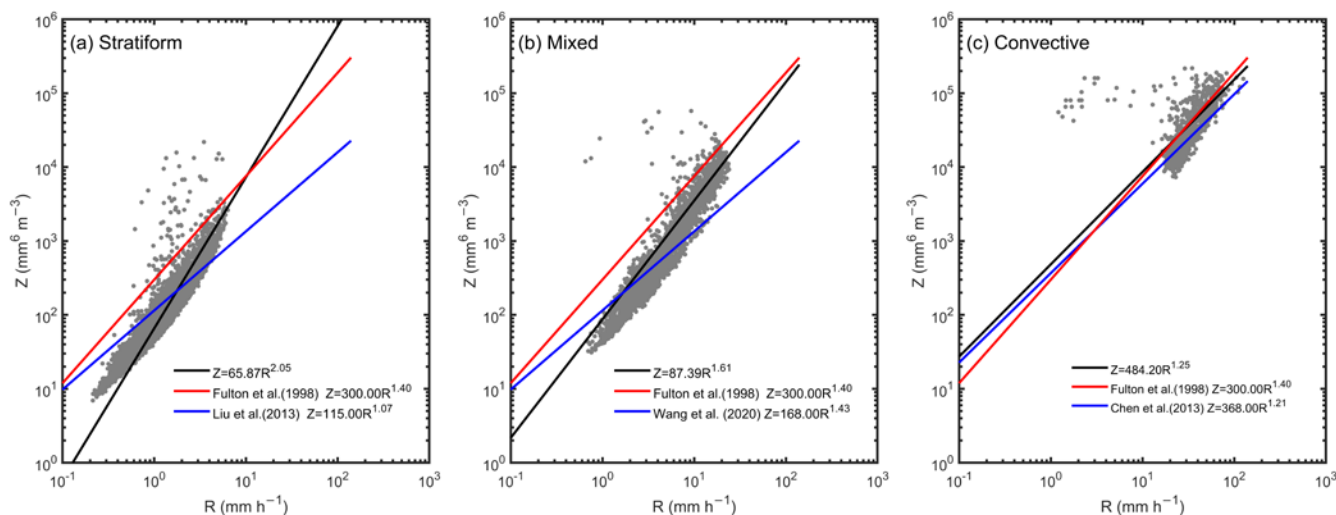


Figure 11. Z – R relationship and the fitted power law relations of different rain types. The red dashed line represents the standard NEXRAD Z – R relationship ($Z = 300R^{1.4}$, Fulton et al., 1998 [30]), and the blue dashed line represents the other fitted power law relations of different rain type obtained by Liu et al., 2013 [55]; Wang et al., 2020 [56]; and Chen et al., 2013 [15], respectively.

3.6. KE – R Relationship

The topography of the southwest mountain area is complex, and precipitation in this region is of significant, sudden, and strong intensity [57]. Heavy precipitation often causes debris flow and landslides in steep mountain areas. Rainfall kinetic energy (KE) can be used as a good indicator to evaluate the damage degree of disasters caused by precipitation. It is usually presented in two forms, namely KE_{time} ($J m^{-2} h^{-1}$) and KE_{mm} ($J m^{-2} mm^{-1}$). Because direct KE measurements are expensive, previous researchers have used alternative methods to measure KE [58,59]. At the same time, using the RSD characteristics obtained by a disdrometer to estimate KE is also a relatively effective method [60]. Many researchers have obtained different relationships between KE and R in many regions based on local RSD information [12,39,61,62]. This suggests that the KE – R relationship is variable. However, the KE – R relationship in the steep terrain of the southwest mountain areas is not clear. Therefore, in this study, it was necessary to use the local RSD information to obtain the KE – R relationship in the southwest mountain areas. For the KE_{time} – R relation, [38] and [60] give the linear and power relations, and, for the KE_{mm} – R relation, they give the power and logarithmic relations of the two. In the above studies, the power relation is the best fit for both KE_{time} – R and KE_{mm} – R . In addition, Wen et al. (2019) fitted the logarithmic relationship of KE_{mm} and R in the study of summer precipitation in Eastern China [12]. In combination with the three studies above, we chose the linear, power, and logarithmic forms to fit our KE – R relationship. The specific information in our study and in the above three studies is shown in Table 5. Figure 12 shows the distribution of KE (KE_{time} and KE_{mm}) in the southwest mountain areas, the fitting relationships of the linear and power functions of KE_{time} – R , and the power and logarithm functions of KE_{mm} – R . For comparison, the KE_{time} – R relationships in the power form for South India [61], the KE_{mm} – R relationships in the logarithmic form for Urumqi and Tianchi [48], and the KE_{mm} – R relationships in the logarithmic form for Nanjing [12] are represented by the dotted line with the corresponding colors in Figure 12. Considering that heavy precipitation mainly occurs in summer, only the KE of the different rain types were analyzed in this paper. It can be seen that the KE_{time} increased with an increase in R . When the R was less than $5 mm h^{-1}$, the KE_{mm} increased sharply, and it increased gently when the R was more than $5 mm h^{-1}$. The linear and power forms of the

KE_{time} - R relationships of the three precipitation types in the southwest mountain areas were all well fitted, with R^2 exceeding 0.95. For KE_{mm} , the fitting effect of the power and exponential forms of stratiform rain and mixed rain was not very good, and the fitting effect of convective rain was better. The R^2 of the two fitting forms was more than 0.6, and the R^2 of the logarithmic form was 0.06 higher than that of the power form. In addition, for a given R , the KE_{time} in the southwest mountain areas was greater than that in South India, and it was greater than that in Urumqi and Tianchi in the case of $R < 50 \text{ mm h}^{-1}$. The KE_{mm} in the study area was greater than that in South India, Urumqi, Tianchi, and Nanjing. Furthermore, considering that there are many mountains in the southwest mountain areas, the terrain is steep, the vegetation coverage rate is not high, and the permeability of the river and the underlying surface is poor. Given the same high R , the larger the KE was in southwest mountain areas, the more likely it was to cause more serious natural disasters, such as landslides and debris flow.

Table 5. Relevant studies on the KE - R relation at various locations [10,38,60].

Reference	Location	KE_{time} - R				KE_{mm} - R			
		Linear: $KE_{time} = aR + b$		Power: $KE_{time} = cR^d$		Power: $KE_{mm} = eR^f$		Log: $KE_{mm} = g \log_{10} R + h$	
		a	b	c	d	e	f	g	h
Present study	Enshi, Southwest China	34.600	1.044	37.710	0.974	33.710	0.069	2.332	33.970
	Urumqi, Northwest China	20.399	-8.765	7.432	1.441	9.762	0.149	2.861	9.789
[60]	Tianchi, Northwest China	24.440	-14.575	7.641	1.415	9.251	0.281	5.299	9.685
[38]	Coast Station, South India	23.408	-29.057	8.838	1.244	10.648	0.175	4.898	11.028
[38]	Inland Station, South India	18.336	-12.372	7.724	1.266	8.588	0.209	4.244	8.925
[10]	Nanjing, Eastern China	-	-	-	-	-	-	5.930	10.120

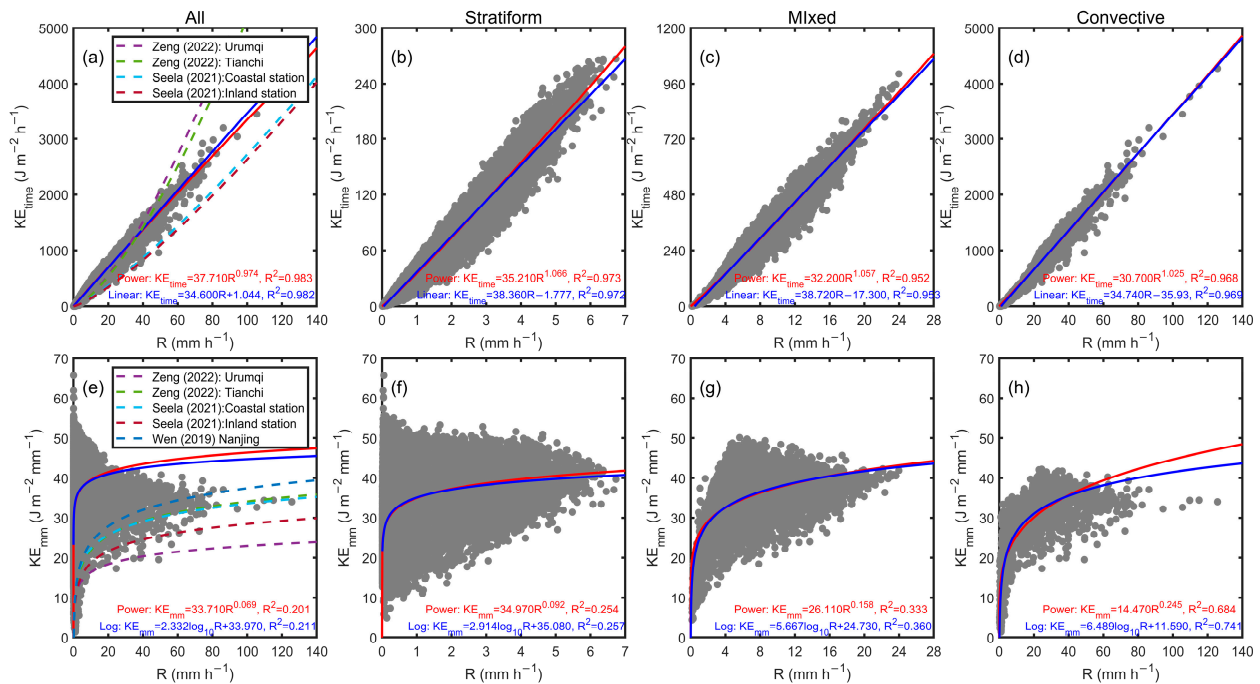


Figure 12. KE_{time} - R (a-d) and KE_{mm} - R (e-h) relationships of the rainfall in the southwest mountain areas. Previous results in Urumqi and Tianchi [60], South India [38], and Nanjing [10] are presented with corresponding colors.

3.7. Comparison of RSD at Different Heights

The RSD characteristics at different heights are sometimes quite different due to the influence of the underlying surface and other factors. How to analyze the differences between them and how to deeply understand the precipitation characteristics is very important. In addition, an in-depth analysis will help in understanding the microphysical process of the clouds and rain at different heights. In this study, a relatively long time and a wide range of precipitation processes in the Hubei Province from June 26 to 28, 2020, were selected to carry out a comparative study on the RSD characteristics at different heights at the top and the foot of the mountain.

In the precipitation process, a total of 1544 min of precipitation data were observed in the southwest mountain areas, 1212 min were observed in Xianfeng Meteorological Station, and 933 min of precipitation data were observed at the same time. A total of 636 min of daytime data (08:00–20:00) and 297 min of night data (08:00–08:00 the next day) were included. As can be seen from Table 6, the R in Xianfeng was significantly higher than that in the southwest mountain areas, and it was $10.22 \text{ mm}^{-1} \text{ h}^{-1}$ higher in the day and $14.81 \text{ mm}^{-1} \text{ h}^{-1}$ higher in the night. In the southwest mountain areas, the R in the daytime was greater than that at night, and the opposite was seen in Xianfeng. Regardless of day or night, the D_m ($\log_{10}N_w$) in Enshi was smaller (greater) than that in Xianfeng. The results indicate that compared to the plains, precipitation in the south mountain areas in summer has more particles of smaller size and higher number concentrations, which may be related to the process of raindrop collision and evaporation caused by the topographic uplift. The D_m and $\log_{10}N_w$ in the Xianfeng area had slight differences between the daytime and night values, which were only 0.01 mm and $0.04 \text{ m}^{-3} \text{ mm}^{-1}$, respectively, while the D_m and $\log_{10}N_w$ in Enshi had a big difference between the night and daytime values, which reached 0.37 mm and $0.63 \text{ mm}^{-1} \text{ m}^{-3}$, respectively. There were slight differences in Z and Λ between Enshi and Xianfeng in the daytime; however, at night, the Z of Xianfeng was 5.92 dBZ higher than that of Enshi, and the Λ of Enshi was 18.05 mm^{-1} higher than that of Xianfeng.

Table 6. Mean microphysical values of Enshi and Xianfeng.

Time	Location	R (mm h^{-1})	D_m (mm)	$\log_{10}N_w$ ($\text{mm}^{-3} \text{ m}^{-1}$)	Z (dBZ)	Λ (mm^{-1})
ALL	Enshi	3.62	1.07	3.98	24.91	19.96
	Xianfeng	15.30	1.37	3.49	26.33	15.30
Day	Enshi	4.10	1.19	3.78	27.03	12.74
	Xianfeng	14.32	1.37	3.47	26.36	14.32
Night	Enshi	2.57	0.82	4.41	20.35	35.43
	Xianfeng	17.38	1.36	3.51	26.27	17.38

Each microphysical parameter was determined by the RSD distribution, which was affected by collision, fragmentation, evaporation, and so on during the falling process, and the RSD distribution changed accordingly. Figure 13 shows the composite raindrop spectra in Enshi and Xianfeng. The number density of raindrops less than 1 mm in the spectral distribution was significantly higher in Enshi than in Xianfeng, especially at night. It is possible that the high wind speed at the top of the mountain made the large raindrops break into smaller raindrops, so the number of small drops at the top of the mountain was very dense. In the process of the raindrops falling, the number density of the small raindrops at the top of the mountain was higher than that at the foot of the mountain because of the interaction between the large raindrops and the small raindrops and the evaporation of the small raindrops. However, the number density of the large raindrops at the foot of the mountain was significantly higher than that at the top of the mountain, which may be because the collision and coalescence process of the raindrops at the foot of the mountain increased the larger raindrops and widened the raindrop spectrum. At the same time, the top of the mountain was in the cloud, and the raindrops did not completely

collide with each other. In addition, the top of the mountain is convex and cone-shaped, and the water supply cloud was easily able to flow around from both sides. Therefore, the collision interaction was not strengthened.

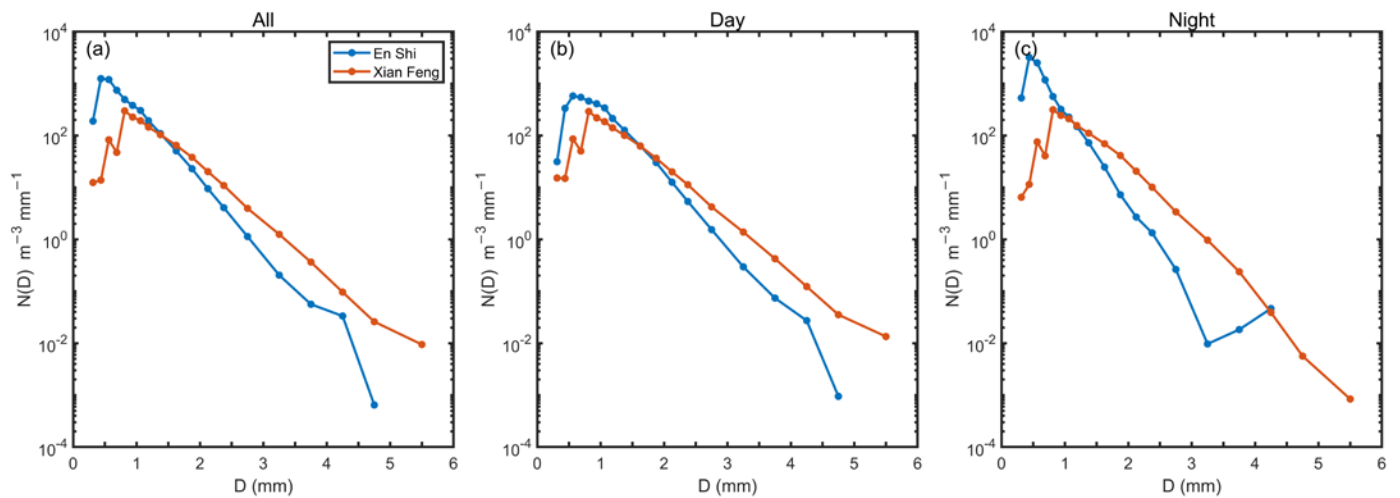


Figure 13. Composite raindrop spectra of all (a), day (b) and night (c) in Enshi and Xianfeng.

To explain the possible reasons for the RSD difference between the mountain and plains, Figure 14 shows the parameters in Enshi and Xianfeng, including air temperature, relative humidity, CAPE, and the vertical integral of the water vapor values. Considering the different altitudes of the two stations, the near-surface pressure of Enshi was about 800 hpa, while that of Xianfeng was about 900 hpa according to the air pressure height formula. Influenced by the elevation difference, during the precipitation process, Xianfeng was obviously hotter and drier than Enshi. Therefore, the evaporation rate of the small raindrops generated by the collision process was higher at the foot of the mountain than at the top of the mountain, resulting in smaller small raindrops arriving at the foot of the mountain than those at the top of the mountain [48]. In addition, Xianfeng had a greater water vapor content and stronger CAPE than Enshi. Deep convection could enhance the aggregation of the ice particles in the cloud, and these larger ice crystals melted when falling and formed larger raindrops [39]. Moreover, the sorting of the raindrops and the strong updraft could keep the small raindrops in the air and prevented them from falling to the ground, which, in turn, provided enough time for the collision process to increase the number of large raindrops by consuming the small ones [63]. The thermodynamic and microphysical processes mentioned above resulted in more small raindrops and less large raindrops at the top of the mountain than at the foot of the mountain, resulting in a larger D_m and lower $\log_{10}N_w$ on the mountain.

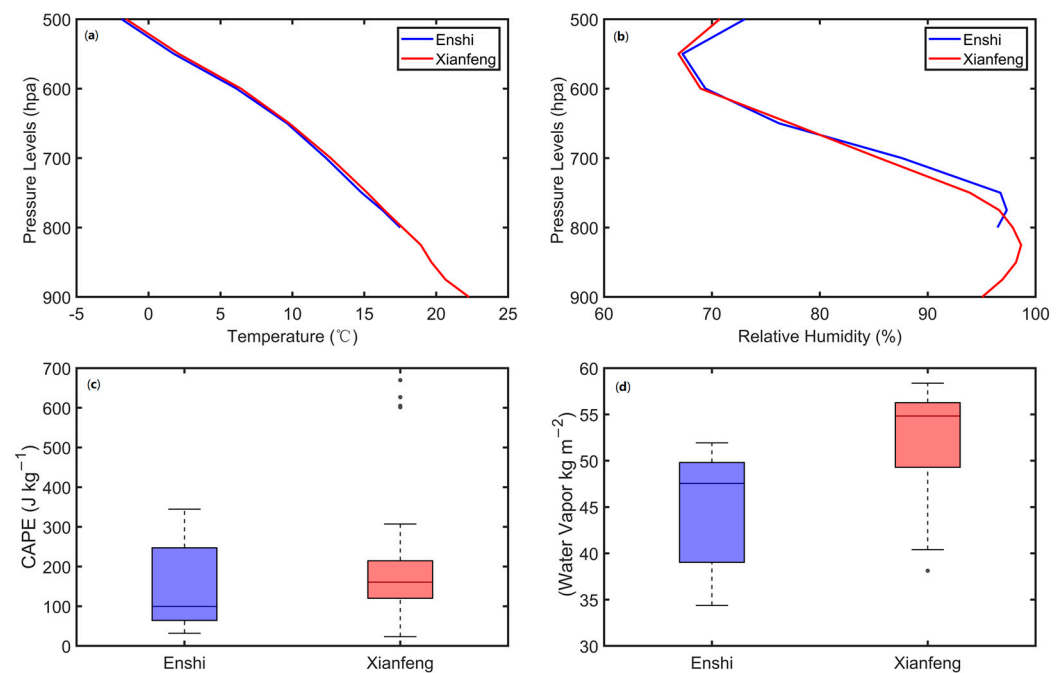


Figure 14. Temperature profiles (a), relative humidity profiles (b), CAPE (c) and water vapor (d) of Enshi and Xianfeng.

4. Discussion

Many previous studies have shown that the RSD varies depending on the rain types, climate characteristics, and geographical location. Additionally, they often focused on the plains, coastal areas, and plateaus, while less research focused on the mountain areas. With the unique mountain climate characteristics and complex terrain in the southwest mountain areas coupled with the influence of the monsoon climate, the weather changes dramatically. Heavy rain, short-time strong precipitation, and freezing rain are common catastrophic weather in this area. Due to this, precipitation is of great significance to the southwest mountain areas. Therefore, it is of great theoretical and practical value to study the characteristics of the RSD, $Z-R$ relationship, and $KE-R$ relationship in the southwest mountain areas.

The two-year observation data of the Enshi Weather Radar Station was studied to reveal the RSD characteristics of the different rain types during the four seasons in the southwest mountain areas. The $\mu-\Lambda$, $Z-R$, and $KE-R$ relationships in this study all showed obvious differences from those in other regions. Although some interesting findings were made on the RSD characteristics in the southwest mountain areas, there were some errors in the results because the small raindrops measured with PARSIVEL² would be smaller than the actual values. The microphysical processes and their differences with respect to different rain types and seasons need further study. We plan to conduct joint observations with more detection equipment as well as to combine GPM satellite and polarized radar data in future studies.

5. Conclusions

Based on the RSD data from 2019 to 2021 in the southwest mountain areas of China, the characteristics of the RSDs of different rain types and of the four seasons were analyzed. Moreover, a typical precipitation process was selected, and the RSD characteristics at different heights were compared with those of Xianfeng at a lower altitude. The main conclusions are as follows:

- (1) Precipitation was mainly stratiform rain in the southwest mountain areas, accounting for 92.7% of the total precipitation time, while the precipitation time of mixed rain and convective rain accounted for 6.1% and 1.6%, respectively. Winter rainfall was

dominated by convective rain (62.9%), while, in the other seasons, the total contribution of mixed rain and stratiform rain to the rainfall amount was more than 80%. The composite raindrop spectra for stratiform rain and mixed rain were unimodal, while that of convective rain was multi-peaked, with their peaks being one or two orders of magnitude higher than those of the plains. The peaks of mixed rain were the highest in all the seasons.

- (2) The D_m of stratiform rain was the smallest, and the $\log_{10}N_w$ of mixed rain was the largest. The convective rain in spring and autumn was very close to the ocean-like convective mass. In winter, the stratiform rain in the southwest mountains had a small D_m and large $\log_{10}N_w$, while convective rain had a large D_m and small $\log_{10}N_w$, reflecting an N_0 jump effect.
- (3) There was a good binomial fitting relationship between the μ and Λ of the RSDs of the three rain types in the southwest mountain areas. Given the same Λ value, the μ - Λ relationship in the southwest mountain areas had a higher μ than that in Florida, which resulted from a higher D_m in the southwest mountain areas. The Z - R relationship varied with geographical location, climatic condition, and rain types. The standard relationship $Z = 300R^{1.4}$ used in the radar estimation of precipitation partially overestimated stratiform rain and mixed rain in the southwest mountain areas, especially stratiform rain. Given the same high R , the KE was larger in the southwest mountain areas than in other areas, which made it more prone to natural disasters.
- (4) The D_m ($\log_{10}N_w$) in the southwest mountains was smaller (greater) than that in Xianfeng, indicating that there were more particles with smaller particle size and higher concentration in summer precipitation in the mountain area. The high wind speed at the top of the mountain made the large raindrops unstable, thus breaking them up into smaller raindrops and resulting in a higher density of small raindrops at the top of the mountain than at the foot of the mountain. A stronger evaporation rate and CAPE as well as a greater water vapor occurred at the foot of the mountain, which strengthened the coagulation between the raindrops and increased the larger droplets, broadening the raindrop size distribution and resulting in a higher density of large droplets at the foot of the mountain than at the top.

Author Contributions: Conceptualization, H.W. and S.N.; methodology, H.W. and S.N.; formal analysis, H.W. and Y.H.; resources, H.W., Y.Z. and J.L.; data curation, H.W. and J.L.; writing—original draft preparation, H.W.; writing—review and editing, H.W.; supervision, S.N.; project administration, H.W. and S.N.; funding acquisition, S.N. and J.S. All authors have read and agreed to the published version of the manuscript.

Funding: This research was funded by the National Natural Science Foundation of China (Grant No. 42075063; No. 42075066) and the Natural Science Foundation of Hubei Province, China (Grant No. 2021CFB571).

Data Availability Statement: Not applicable.

Acknowledgments: The first author thanks Wanting Qin for polishing the manuscript. The authors would like to thank the Institute of Heavy Rain, CMA, Wuhan for providing the data of the disdrometers. Thanks also go to the reviewers for their thorough comments that really helped to improve the manuscript.

Conflicts of Interest: The authors declare no conflict of interest.

References

1. Rosenfeld, D.; Ulbrich, C.W. Cloud microphysical properties, processes, and rainfall estimation opportunities. *Meteor. Monogr.* **2003**, *30*, 237–258. [[CrossRef](#)]
2. Das, S.K.; Konwar, M.; Chakravarty, K.; Deshpande, S.M. Raindrop size distribution of different cloud types over the Western Ghats using simultaneous measurements from Micro-Rain Radar and disdrometer. *Atmos. Res.* **2017**, *186*, 72–82. [[CrossRef](#)]
3. Iguchi, T.; Matsui, T.; Tokay, A.; Kollias, P.; Tao, W.-K. Two distinct modes in one-day rainfall event during MC3E field campaign: Analyses of disdrometer observations and WRF-SBM simulation. *Geophys. Res. Lett.* **2012**, *39*, L24805. [[CrossRef](#)]

4. Maki, M.; Keenan, T.D.; Sasaki, Y.; Nakamura, K. Characteristics of the Raindrop Size Distribution in Tropical Continental Squall Lines Observed in Darwin, Australia. *J. Appl. Meteorol.* **2001**, *40*, 1393–1412. [[CrossRef](#)]
5. Sui, C.-H.; Tsay, C.-T.; Li, X. Convective–stratiform rainfall separation by cloud content. *J. Geophys. Res. Atmos.* **2007**, *112*, D14213. [[CrossRef](#)]
6. Houze, R.A., Jr. *Cloud Dynamics*, 2nd ed.; Academic Press: Oxford, UK, 2014.
7. Tokay, A.; Short, D.A. Evidence from Tropical Raindrop Spectra of the Origin of Rain from Stratiform versus Convective Clouds. *J. Appl. Meteorol.* **1996**, *35*, 355–371. [[CrossRef](#)]
8. Bringi, V.N.; Chandrasekar, V.; Hubbert, J.; Gorgucci, E.; Randeu, W.L.; Schoenhuber, M. Raindrop Size Distribution in Different Climatic Regimes from Disdrometer and Dual-Polarized Radar Analysis. *J. Atmos. Sci.* **2003**, *60*, 354–365. [[CrossRef](#)]
9. Thurai, M.; Gatlin, P.N.; Bringi, V.N. Separating stratiform and convective rain types based on the drop size distribution characteristics using 2D video disdrometer data. *Atmos. Res.* **2016**, *169 Pt B*, 416–423. [[CrossRef](#)]
10. Zeng, Q.; Zhang, Y.; Lei, H.; Xie, Y.; Gao, T.; Zhang, L.; Wang, C.; Huang, Y. Microphysical Characteristics of Precipitation during Pre-monsoon, Monsoon, and Post-monsoon Periods over the South China Sea. *Adv. Atmos. Sci.* **2019**, *36*, 1103–1120. [[CrossRef](#)]
11. Tang, Q.; Xiao, H.; Guo, C.; Feng, L. Characteristics of the raindrop size distributions and their retrieved polarimetric radar parameters in northern and southern China. *Atmos. Res.* **2014**, *135–136*, 59–75. [[CrossRef](#)]
12. Wen, L.; Zhao, K.; Wang, M.; Zhang, G. Seasonal Variations of Observed Raindrop Size Distribution in East China. *Adv. Atmos. Sci.* **2019**, *36*, 346–362. [[CrossRef](#)]
13. Chen, B.; Hu, Z.; Liu, L.; Zhang, G. Raindrop Size Distribution Measurements at 4500 m on the Tibetan Plateau During TIPEX-III. *J. Geophys. Res. Atmos.* **2017**, *122*, 11092–11106. [[CrossRef](#)]
14. Gatlin, P.N.; Thurai, M.; Bringi, V.N.; Petersen, W.; Wolff, D.; Tokay, A.; Carey, L.; Wingo, M. Searching for Large Raindrops: A Global Summary of Two-Dimensional Video Disdrometer Observations. *J. Appl. Meteorol. Climatol.* **2015**, *54*, 1069–1089. [[CrossRef](#)]
15. Chen, B.; Yang, J.; Pu, J. Statistical Characteristics of Raindrop Size Distribution in the Meiyu Season Observed in Eastern China. *J. Meteorol. Soc. Jpn.* **2013**, *91*, 215–227. [[CrossRef](#)]
16. Ushiyama, T.; Krishna Reddy, K.; Kubota, H.; Yasunaga, K.; Shirooka, R. Diurnal to interannual variation in the raindrop size distribution over Palau in the western tropical Pacific. *Geophys. Res. Lett.* **2009**, *36*, L02810. [[CrossRef](#)]
17. Chen, B.; Wang, J.; Gong, D. Raindrop Size Distribution in a Midlatitude Continental Squall Line Measured by Thies Optical Disdrometers over East China. *J. Appl. Meteorol. Clim.* **2016**, *55*, 621–634. [[CrossRef](#)]
18. Suh, S.-H.; You, C.-H.; Lee, D.-I. Climatological characteristics of raindrop size distributions in Busan, Republic of Korea. *Hydrol. Earth Syst. Sci.* **2016**, *20*, 193–207. [[CrossRef](#)]
19. Porcù, F.; D’Adderio, L.P.; Prodi, F.; Caracciolo, C. Rain drop size distribution over the Tibetan Plateau. *Atmos. Res.* **2014**, *150*, 21–30. [[CrossRef](#)]
20. Levin, Z.; Feingold, G.; Tzivion, S.; Waldvogel, A. The Evolution of Raindrop Spectra: Comparisons between Modeled and Observed Spectra along a Mountain Slope in Switzerland. *J. Appl. Meteorol.* **1991**, *30*, 893–900. [[CrossRef](#)]
21. Löffler-Mang, M.; Joss, J. An Optical Disdrometer for Measuring Size and Velocity of Hydrometeors. *J. Atmos. Ocean. Technol.* **2000**, *17*, 130–139. [[CrossRef](#)]
22. Tokay, A.; Wolff, D.B.; Petersen, W.A. Evaluation of the New Version of the Laser-Optical Disdrometer, OTT PARSIVEL2. *J. Atmos. Ocean. Technol.* **2014**, *31*, 1276–1288. [[CrossRef](#)]
23. Wen, L. Microphysical Characteristics of the Raindrop Size Distribution Observed in East China during the Asian Summer Monsoon Season. Master’s Thesis, Nanjing University, Nanjing, China, 2016. (In Chinese).
24. Fu, Z.; Dong, X.; Zhou, L.; Cui, W.; Wang, J.; Wan, R.; Leng, L.; Xi, B. Statistical Characteristics of Raindrop Size Distributions and Parameters in Central China during the Meiyu Seasons. *J. Geophys. Res. Atmos.* **2020**, *125*, e2019JD031954. [[CrossRef](#)]
25. Jia, X.; Liu, Y.; Ding, D.; Ma, X.; Chen, Y.; Bi, K.; Tian, P.; Lu, C.; Quan, J. Combining disdrometer, microscopic photography, and cloud radar to study distributions of hydrometeor types, size and fall velocity. *Atmos. Res.* **2019**, *228*, 176–185. [[CrossRef](#)]
26. Gunn, R.; Kinzer, G.D. The terminal velocity of fall for water drops in stagnant air. *J. Atmos. Sci.* **1949**, *6*, 243–248.
27. Locatelli, J.D.; Hobbs, P.V. Fall speeds and masses of solid precipitation particles. *J. Geophys. Res. Atmos.* **1974**, *79*, 2185–2197. [[CrossRef](#)]
28. Niu, S.; Jia, X.; Sang, J.; Liu, X.; Lu, C.; Liu, Y. Distributions of Raindrop Sizes and Fall Velocities in a Semiarid Plateau Climate: Convective versus Stratiform Rains. *J. Appl. Meteorol. Clim.* **2010**, *49*, 632–645. [[CrossRef](#)]
29. Wen, L.; Zhao, K.; Zhang, G.; Xue, M.; Zhou, B.; Liu, S.; Chen, X. Statistical characteristics of raindrop size distributions observed in East China during the Asian summer monsoon season using 2-D video disdrometer and Micro Rain Radar data. *J. Geophys. Res. Atmos.* **2016**, *121*, 2265–2282. [[CrossRef](#)]
30. Ulbrich, C.W. Natural Variations in the Analytical Form of the Raindrop Size distribution. *J. Clim. Appl. Meteorol.* **1983**, *22*, 1764–1775. [[CrossRef](#)]
31. Vivekanandan, J.; Zhang, G.; Brandes, E. Polarimetric Radar Estimators Based on a Constrained Gamma Drop Size Distribution Model. *J. Appl. Meteorol.* **2004**, *43*, 217–230. [[CrossRef](#)]
32. Bringi, V.N.; Williams, C.R.; Thurai, M.; May, P.T. Using dual-polarized radar and dual-frequency profiler for dsd characterization: A case study from Darwin, Australia. *J. Atmos. Ocean. Technol.* **2009**, *26*, 2107. [[CrossRef](#)]

33. Ding, Y.H.; Liu, Y.J.; Sun, Y.; Song, Y.F. Weakening of the Asian summer monsoon and its impact on the precipitation pattern in China. *Int. J. Water Resour. Dev.* **2010**, *26*, 423–439. [[CrossRef](#)]
34. Huang, Z.W.; Peng, S.Y.; Zhang, H.R.; Zheng, J.F.; Zeng, Z.M.; Wang, Y.J. Characteristics of raindrop size distribution at Anxi of Fujian. *J. Appl. Meteor. Sci.* **2022**, *33*, 205–217. (In Chinese)
35. Smith, R.K. *The Physics and Parameterization of Moist Atmospheric Convection*; Springer: Berlin/Heidelberg, Germany, 1997; 2176p.
36. Li, H.; Yin, Y.; Shan, Y.; Jin, Q. Statistical characteristics of raindrop size distribution for stratiform and convective precipitation at different altitudes in Mt. Huangshan. *Chin. J. Atmos. Sci.* **2018**, *42*, 268–280. (In Chinese)
37. Guo, L.J.; Guo, X.L.; Lou, X.F.; Lu, G.X.; Lyu, K.; Sun, H.M.; Li, J.; Zhang, X.P. An observational study of diurnal and seasonal variations, and macroscopic and microphysical properties of clouds and precipitation over Mount Lu, Jiangxi, China. *Acta Meteorol. Sin.* **2019**, *77*, 923–937. (In Chinese)
38. Fang, B.; Guo, X.; Xiao, H. A study on characteristics of spectral parameters and characteristic variables of raindrop size distribution for different cloud systems in Liaoning Province. *Chin. J. Atmos. Sci.* **2020**, *40*, 1154–1164. (In Chinese)
39. Seela, B.K.; Janapati, J.; Lin, P.-L.; Wang, P.K.; Lee, M.-T. Raindrop Size Distribution Characteristics of Summer and Winter Season Rainfall over North Taiwan. *J. Geophys. Res. Atmos.* **2018**, *123*, 11–602. [[CrossRef](#)]
40. Waldvogel, A. The N_0 jump of raindrop spectra. *J. Atmos. Sci.* **1974**, *31*, 1067–1078. [[CrossRef](#)]
41. Dolan, B.; Fuchs, B.; Rutledge, A.; Barnes, E.A.; Thompson, E.J. Primary Modes of Global Drop Size Distributions. *J. Atmos. Sci.* **2018**, *75*, 1453–1476. [[CrossRef](#)]
42. Milbrandt, J.A.; Yau, M.K. A multimoment bulk microphysics parameterization. Part I: Analysis of the role of the spectral shape parameter. *J. Atmos. Sci.* **2005**, *62*, 3051–3064.
43. Zhang, G.; Vivekanandan, J.; Brandes, E. A method for estimating rain rate and drop size distribution from polarimetric radar measurements. *IEEE Trans. Geosci. Remote Sens.* **2001**, *39*, 830–841. [[CrossRef](#)]
44. Thurai, M.; Bringi, V.N.; May, P.T. CPOL Radar-Derived Drop Size Distribution Statistics of Stratiform and Convective Rain for Two Regimes in Darwin, Australia. *J. Atmos. Ocean. Technol.* **2010**, *27*, 932–942. [[CrossRef](#)]
45. Zhang, G.; Vivekanandan, J.; Brandes, E.A.; Meneghini, R.; Kozu, T. The Shape–Slope Relation in Observed Gamma Raindrop Size Distributions: Statistical Error or Useful Information? *J. Atmos. Ocean. Technol.* **2003**, *20*, 1106–1119. [[CrossRef](#)]
46. Chu, Y.-H.; Su, C.-L. An Investigation of the Slope–Shape Relation for Gamma Raindrop Size Distribution. *J. Appl. Meteorol. Clim.* **2008**, *47*, 2531–2544. [[CrossRef](#)]
47. Chang, W.-Y.; Wang, T.-C.C.; Lin, P.-L. Characteristics of the Raindrop Size Distribution and Drop Shape Relation in Typhoon Systems in the Western Pacific from the 2D Video Disdrometer and NCU C-Band Polarimetric Radar. *J. Atmos. Ocean. Technol.* **2009**, *26*, 1973–1993. [[CrossRef](#)]
48. Zeng, Y.; Yang, L.M.; Zhou, Y.S.; Tong, Z.P.; Jiang, Y.F.; Chen, P. Characteristics of orographic raindrop size distribution in the Tianshan Mountains, China. *Atmos. Res.* **2022**, *278*, 106332. [[CrossRef](#)]
49. Seela, B.K.; Janapati, J.; Lin, P.-L.; Lan, C.-H.; Shirooka, R.; Hashiguchi, H.; Reddy, K.K. Raindrop size distribution characteristics of the western Pacific tropical cyclones measured in the Palau islands. *Remote Sens.* **2022**, *14*, 470. [[CrossRef](#)]
50. Cao, Q.; Zhang, G.; Brandes, E.; Schuur, T.; Ryzhkov, A.; Ikeda, K. Analysis of video disdrometer and polarimetric radar data to characterize rain microphysics in Oklahoma. *J. Appl. Meteorol. Clim.* **2008**, *47*, 2238–2255. [[CrossRef](#)]
51. Chandrasekar, V.; Meneghini, R.; Zawadzki, I. Global and Local Precipitation Measurements by Radar. *Meteorol. Monogr.* **2003**, *30*, 215. [[CrossRef](#)]
52. Zheng, H.; Wu, Z.; Zhang, L.; Xie, Y.; Lei, H. Improving Radar Rainfall Estimations with Scaled Raindrop Size Spectra in Mei-Yu Frontal Rainstorms. *Sensors* **2020**, *20*, 5257. [[CrossRef](#)]
53. Fulton, R.A. Sensitivity of WSR-88D Rainfall Estimates to the Rain-Rate Threshold and Rain Gauge Adjustment: A Flash Flood Case Study. *Weather. Forecast.* **1999**, *14*, 604–624. [[CrossRef](#)]
54. Zhang, P.; Liu, X.; Zhou, Z.; Song, K.; Yang, P. Research on Precipitation Estimators of Microwave Link and Weather Radar Based on Raindrop Size Distribution Data. *Meteor. Mon.* **2021**, *47*, 843–853. (In Chinese)
55. Liu, Y. Analysis on Microphysical Characteristics of Convective and Stratiform Cloud Precipitation in Beijing. Master’s Thesis, Nanjing University of Information Science and Technology, Nanjing, China, 2013. (In Chinese).
56. Wang, J.; Yue, Z.; He, W.; Dai, C.; Pang, L.; Liu, H.; Zhang, L. Research on the Z-R relationship of mixed convective-stratiform clouds in Xi’an area. *Torrential Rain Disasters* **2020**, *39*, 409–417. (In Chinese)
57. Luo, Y.; Wu, M.; Ren, F.; Li, J.; Wong, W.-K. Synoptic Situations of Extreme Hourly Precipitation over China. *J. Clim.* **2016**, *29*, 8703–8719. [[CrossRef](#)]
58. Kinnell, P.I.A. Rainfall Intensity-Kinetic Energy Relationships for Soil Loss Prediction. *Soil Sci. Soc. Am. J.* **1981**, *45*, 153. [[CrossRef](#)]
59. Jayawardena, A.W.; Rezaur, R.B. Measuring drop size distribution and kinetic energy of rainfall using a force transducer. *Hydrol. Process.* **2000**, *14*, 37–49. [[CrossRef](#)]
60. Fornis, R.L.; Vermeulen, H.R.; Nieuwenhuis, J.D. Kinetic energy–rainfall intensity relationship for Central Cebu, Philippines for soil erosion studies. *J. Hydrol.* **2005**, *300*, 20–32. [[CrossRef](#)]
61. Seela, B.K.; Janapati, J.; Kalath Unnikrishnan, C.; Lin, P.-L.; Le Loh, J.; Chang, W.-Y.; Kumar, U.; Reddy, K.K.; Lee, D.-I.; Reddy, M.V. Raindrop size distributions of North Indian Ocean tropical cyclones observed at the coastal and inland stations in South India. *Remote Sens.* **2021**, *13*, 3178. [[CrossRef](#)]

62. Steiner, M.; Smith, J.A. Reflectivity, Rain Rate, and Kinetic Energy Flux Relationships Based on Raindrop Spectra. *J. Appl. Meteorol.* **2000**, *39*, 1923–1940. [[CrossRef](#)]
63. Hu, Z.; Srivastava, R.C. Evolution of raindrop size distribution by coalescence, breakup, and evaporation: Theory and observations. *J. Atmos. Sci.* **1995**, *52*, 1761–1783. [[CrossRef](#)]

Disclaimer/Publisher’s Note: The statements, opinions and data contained in all publications are solely those of the individual author(s) and contributor(s) and not of MDPI and/or the editor(s). MDPI and/or the editor(s) disclaim responsibility for any injury to people or property resulting from any ideas, methods, instructions or products referred to in the content.